Spatio-temporal Convergence of Maximum Daily Light-Use Efficiency Based on Radiation Absorption by Canopy Chlorophyll

Yao Zhang[1,*], Xiangming Xiao[1,2,*], Sebastian Wolf[3], Jin Wu[4], Xiaocui Wu[1], Beniamino Gioli[5], Georg Wohlfahrt[6], Alessandro Cescatti[7], Christiaan van der Tol[8], Sha Zhou[9], Christopher M. Gough[10], Pierre Gentine[11], Yongguang Zhang[12], Rainer Steinbrecher[13], Jonas Ardö[14]

[1]Department of Microbiology and Plant Biology, Center for Spatial Analysis, University of Oklahoma, Norman, OK 73019, USA

[2]Ministry of Education Key Laboratory of Biodiversity Science and Ecological Engineering, Institute of Biodiversity Science, Fudan University, Shanghai, 200433, China

[3]Department of Environmental Systems Science, ETH Zurich, 8092 Zurich, Switzerland

[4]Biological, Environmental & Climate Sciences Department, Brookhaven National Lab, Upton, 41 New York, NY 11973

[5]National Research Council—Institute of Biometeorology, via Giovanni Caproni 8—I-50145 Firenze, Italy

[6]University of Innsbruck, Institute of Ecology, Sternwartestraße 15, A-6020 Innsbruck, Austria

[7]European Commission, Joint Research Centre, Directorate for Sustainable Resources, Ispra, Italy

[8]Department of Water Resources, Faculty ITC, University of Twente, 7500 Enschede, The Netherlands

[9]State Key Laboratory of Hydroscience and Engineering, Department of Hydraulic Engineering, Tsinghua University, Beijing, China

[10]Virginia Commonwealth University, Department of Biology, Richmond, VA 23284-2012, USA

[11]Department of Earth and Environmental Engineering, Columbia University, New York, New York, 10027, USA

[12]Jiangsu Center for Collaborative Innovation in Geographical Information Resource Development and Application, International Institute for Earth System Sciences, Nanjing University, 210023 Nanjing, China

[13]Department of Atmospheric Environmental Research, Institute for Meteorology and Climate Research, Karlsruhe Institute of Technology, Kreuzeckbahnstr. 19, 82467 Garmisch-Partenkirchen, Germany

[14]Physical Geography and Ecosystem Science, Lund University. Sölvegatan 12, SE-223 62 Lund, Sweden

Contents of this file

Additional Supporting Information (Files uploaded separately)

Captions for Tables S2

Introduction

This supporting information include a detailed justification of the use of SIF as a proxy of $APAR_{chl}$ (Text S1), data quality check for satellite and flux data (Text S2), the error propagation analysis (Text S3) and the landcover map used in this study (Text S4). It also includes 11 figures and 6 tables to support the analysis.

Text S1 Relationship between SIF and $fPAR_{chl}$.

We use the soil-canopy spectral radiances, photosynthesis, fluorescence, temperature and energy fluxes (SCOPE) model (*van der Tol et al.*, 2009b) to explore the robustness of using SIF to derive $fPAR_{chl}$. The SCOPE model simulates (1) the distribution of incident light over leaves as a function of leaf position in the canopy and leaf orientation, (2) the conversion of incident light on leaves into fluorescence emission spectra, and (3) the propagation of fluorescence through the canopy. At the leaf level, it also simulates photosynthesis as a function of irradiance, leaf temperature, humidity and CO_2 concentration. For the first step, the 'Scattering of Arbitrary Inclined Leaves' (SAIL) model (*Verhoef*, 1984) concept is used, and for the second step, the Fluspect model (*Verhoef*, 2011), a model that simulates the probability of the light absorbed by chlorophyll to four sinks, i.e., photochemistry (ϕ_P), fluorescence (ϕ_F), heat dissipation in light-adapted condition (ϕ_N) and dark-adapted condition (ϕ_D), is used. For the third step, the FluorSAIL model simulates the reabsorption of fluorescence in the canopy that reduce the fluorescence to a value that is lower than the total emitted fluorescence by all leaves; this reabsorption can be characterized using a factor f_{esc}. In essence, the simulated photosynthesis summed over all leaves (A) and the simulated observation of SIF can be expressed as:

$$A = \phi_p \times fPAR_{chl} \times PAR$$
$$SIF = \phi_f \times fPAR_{chl} \times PAR \times f_{esc}$$

The integration of the $\phi_F \times f_{esc}$ of the canopy equals to fluorescence efficiency (FE) in Eq. 2. To test whether FE can be approximated as a constant, we tested the variation of the two components of FE, i.e., ϕ_F and f_{esc}, comparing with the variation of APAR_{chl} ($\text{fPAR}_{chl} \times \text{PAR}$). Previous studies suggest the maximum carboxylation rate (V_{cmax}) is one of the most important factor which determines the probability of the partitioning of the absorbed photon by chlorophyll (ϕ_F) (*van der Tol et al.*, 2009a; *Y Zhang et al.*, 2014). We first ran the SCOPE model using different V_{cmax} values for one vegetation type (LAI = 3, Cab = 80 $\mu g\ cm^{-2}$) over different values of irradiance (thus constant f_{esc} but variable PAR) and showed that the ϕ_F can be considered as a first approximation as a constant (Fig. S3), because the variability of APAR_{chl} is much larger than that of ϕ_F. As SIF is also sensitive to chlorophyll a+b content (Cab), dry matter content (Cdm) and leaf area index (LAI) (*Verrelst et al.*, 2015), which may alter SIF through the change of f_{esc}. We then ran SCOPE for one value of irradiance but different value of Cab, Cdm and LAI (thus constant PAR but variable f_{esc}) (Table S6), we found that the FE has much less variation (2.04$\pm$0.34 J nm^{-1} sr^{-1} mol^{-1}) (Fig. S4) compared to the fPAR$_{chl}$ (0.57$\pm$0.18). Considering the PAR variation during the satellite overpass, the total variation of APAR$_{chl}$ will be much higher than f_{esc}. Because both ϕ_F and f_{esc} have much smaller variation compared with APAR$_{chl}$, FE can be considered as a first approximation as a constant.

Text S2. Data quality check for FLUXNET2015 and remote sensing dataset

For FLUXNET2015 dataset, we applied the following screening rules to increase confidence: (1) For each 8-day (10-day) interval, we filtered out all periods with less than 75% of good quality (based on daily quality check field) gap-filled data of shortwave radiation and NEE observation. (2) To reduce the uncertainties of the flux partitioning, we compared the GPP estimates from both daytime and nighttime partitioning methods on 8-day (10-day) periods and excluded those with more than 10% difference between methods.

We applied a rigorous data quality checks for three MODIS product, when comparing with fPAR$_{SIF}$ at global scale to determine the best fPAR$_{chl}$ proxies, only the highest quality observations are used for analysis: for NDVI and EVI, we only used quality layer Pixel Reliability = 0, (Good Data); for fPAR$_{mod15}$, we used same quality check method as described below in the site level analysis below; for MTCI, we masked out those areas that were identified as bad quality by MODIS data quality layer. The bad quality layers were also applied to fPAR$_{SIF}$ so that the area used to calculate the average value of OVAIs for each month were also used to calculate the average value for fPAR$_{SIF}$. We also filtered the regions with persistent high cloud cover (since high cloud cover would invalidate our use of cos(SZA) as a proxy of PAR), and those regions with very low signal to noise ratio (e.g. barren area).

To compare with the site-level eddy covariance measurements, four OVAIs were undergone rigorous data quality check: (1) The robustness of MODIS VIs (i.e., NDVI, EVI) retrievals was checked using the quality control layer from MOD09A1 C6; observations affected by cloud ("internal cloud algorithm flag" equals to "1"), high or climatological aerosols ("aerosol quantity" equals to "00" or "11"), and snow ("internal snow mask" equals to "1") were eliminated (*Vermote*, 2015). For the MOD15A2H C6 fPAR product (fPAR$_{mod15}$), the additional five-level confidence score was evaluated

("SCF_QC" equals to "000" or "001"), and only observations using the main algorithms (radiative transfer model) were retained (*Myneni et al.*, 2015). (2) The BISE algorithm (*Viovy et al.*, 1992) was applied to remove values that were potentially biased by atmospheric conditions and that were not identified by previous quality checks. (3) The remaining high-quality values were then linearly interpolated to fill the gaps created from the previous steps. For MTCI, we did not apply any quality check procedure and just replaced all zero values with NAs during the analysis as no quality control layer is provided by the data product.

Text S3. Error propagation in each approximation

Since our study includes several comparisons and approximations, the uncertainties related to each dataset and approximations can affect the final result. Therefore, we analyzed the uncertainties using the error propagation law (Deming, 1943):

$$\sigma_f{}^2 = \mathbf{g}^{\mathrm{T}}\mathbf{V}\mathbf{g}$$

Here $\sigma_f{}^2$ represents the variance of the function f with a set of parameters $\boldsymbol{\beta}$, whose variance-covariance matrix is $\mathbf{V}$. The ith element in the vector $\mathbf{g}$ is $\frac{\partial f}{\partial \beta_i}$. If the parameters in vector $\boldsymbol{\beta}$ are uncorrelated, the error propagation can be simplified to:

$$\sigma_f{}^2 = \sum \left(\frac{\partial f}{\partial \beta_i}\right)^2 \sigma_{\beta_i}{}^2$$

This equation allows us to calculate the variance of a function ($\sigma_f{}^2$) from the variance of its individual input ($\sigma_{\beta_i}{}^2$). The uncertainties of a variable can be greatly reduced by averaging n measurements:

$$\sigma_{\bar{f}}{}^2 = \frac{\sigma_f{}^2}{n}$$

The error propagation for a linear regression can be quantified from two aspects: (1) the uncertainty of the regression, which can be quantified as an error term ϵ (Fig. S9), and (2) the uncertainty from the independent variable. A detailed error propagation calculation can be found below, and the uncertainties for each step are summarized in Table S3.

There are two major approximations in our analyses: (1) using SIF as an approximation of fPAR$_{chl}$ (fPAR$_{SIF}$). (2) using OVAIs as approximations of fPAR$_{chl}$ (fPAR$_{SIF}$). In this error propagation analysis, the uncertainties of fPAR$_{chl}$ and fPAR$_{SIF}$ are same in terms of CV, since the uncertainties in ϕ_f and f_{esc} are also considered for fPAR$_{SIF}$. For the first step of approximation, fPAR$_{chl}$ can be expressed as:

$$\mathrm{fPAR_{chl}} = \frac{\mathrm{SIF}}{\mathrm{iPAR} \times \phi_f \times f_{esc}}$$

The uncertainty of fPAR$_{SIF}$ ($\sigma_{\mathrm{fPAR_{SIF}}}$) can be calculated from the uncertainties from each independent variable using the error propagation law and assuming each independent variable is independent from each other:

$$\frac{\sigma_{\mathrm{fPAR_{SIF}}}}{\mathrm{fPAR_{SIF}}} = \frac{\sigma_{\mathrm{fPAR_{chl}}}}{\mathrm{fPAR_{chl}}} = \sqrt{\left(\frac{\sigma_{\mathrm{SIF}}}{\mathrm{SIF}}\right)^2 + \left(\frac{\sigma_{\mathrm{iPAR}}}{\mathrm{iPAR}}\right)^2 + \left(\frac{\sigma_{\phi_f}}{\phi_f}\right)^2 + \left(\frac{\sigma_{f_{esc}}}{f_{esc}}\right)^2}$$

where $\frac{\sigma_{iPAR}}{iPAR}$ can be calculated from the approximation of cos(SZA) (Fig. S10), $\frac{\sigma_{\phi_f}}{\phi_f}$ and $\frac{\sigma_{fesc}}{f_{esc}}$ can be obtained from the SCOPE simulation.

To evaluate the performance of the four OVAIs as proxies of fPAR$_{SIF}$, we first spatially averaged the both fPAR$_{SIF}$ and each OVAIs for each month. This average will greatly reduce the uncertainty in both fPAR$_{SIF}$ and OVAIs. Except for the cropland in Southern Hemisphere which only include 382 $0.5° \times 0.5°$ gridcells, all other biome types have at least 2000 gridcells. which will reduce the uncertainty of fPAR$_{SIF}$ to around or less than 0.01 CV ($0.45/\sqrt{2000}$). The uncertainties of the OVAIs in this comparison is also less than 0.01 CV. Therefore, the uncertainties from the data sources of this comparison (Fig. 1) are ignored.

The uncertainties of using OVAIs as a proxy of fPAR$_{SIF}$ come from two major aspects: (1) the uncertainty in the linear regression, which can be quantified as an error term ϵ, and (2) the uncertainty in the independent variables, i.e., OVAIs. The fPAR$_{SIF}$ can be expressed as:

$$fPAR_{SIF} = a \times (OVAI - c) + \epsilon$$

Or using OVAI$_m$ as the proxy of fPAR$_{chl}$:

$$OVAI_m = OVAI - c + \frac{\epsilon}{a}$$

The error term ϵ for each OVAI can be estimated from the linear regression between fPAR$_{SIF}$ and OVAIs with fixed intercepts c (0.2 for fPAR$_{mod15}$ and NDVI, 0.1 for EVI and 1 for MTCI, Fig. S6). The uncertainty of fPAR$_{SIF}$ (fPAR$_{chl}$) estimated from OVAIs (OVAI$_m$) can be calculated from below:

$$\sigma_{OVAI_m} = \sqrt{\sigma_{OVAI}{}^2 + \left(\frac{\sigma_\epsilon}{a}\right)^2}$$

Since we used five 8-day (four 10-day for MTCI) average of OVAI$_m$ to compare with LUE$_{eco}$, this average will reduce the uncertainty contributed from the OVAI (σ_{OVAI}). The adjusted uncertainty (σ_{OVAI_m}') is calculated below:

$$\sigma_{OVAI_m}' = \sqrt{\frac{\sigma_{OVAI}{}^2}{n} + \left(\frac{\sigma_\epsilon}{a}\right)^2}$$

where n is 5 for fPAR$_{mod15}$, NDVI and EVI, and 4 for MTCI. The result for these uncertainties are shown in Table S3.

The uncertainties of regression slopes in LUE$_{canopy}$ and LUE$_{chl}$ estimation comes from both the uncertainty in GPP from flux tower, and the uncertainty of fPAR$_{canopy}$ and fPAR$_{chl}$ (OVAI$_m$). For a linear regression equation which passes the origin (0, 0) $y = ax$, the regression slope a can be calculated as:

$$a = \frac{\sum x_i y_i}{\sum x_i{}^2}$$

Based on the error propagation law, the uncertainty of a caused by the uncertainty of x (σ_x) and y (σ_y) will be estimated as:

5

$$\sigma_a{}^2 = \sum_{j=1}^{n} \left(\frac{\partial a}{\partial x_j} \sigma_{x_j} \right)^2 + \sum_{j=1}^{n} \left(\frac{\partial a}{\partial y_j} \sigma_{y_j} \right)^2$$

$$= \sum_{j=1}^{n} \left(\frac{y_j}{\sum_{i=1}^{n} x_i{}^2} - \frac{2x_j}{\left(\sum_{i=1}^{n} x_i{}^2 \right)^2} \right)^2 \sigma_{x_j}{}^2 + \sum_{j=1}^{n} \left(\frac{x_j}{\sum_{i=1}^{n} x_i{}^2} \right)^2 \sigma_{y_j}{}^2$$

where the uncertainty of y_j (σ_{y_j}) is regarded as 10% of y (LUE$_{eco}$); the uncertainty of x_j (σ_{x_j}) is a fixed value from Table S3.

The CV is used to evaluate how convergent of the different definition of LUE (LUE$_{eco}$, LUE$_{canopy}$, LUE$_{chl}$), and can be calculated as:

$$CV = \frac{\sqrt{\dfrac{\sum_{i=1}^{n}(l_i - \bar{l})^2}{n - 1}}}{\bar{l}}$$

where $\bar{l}$ is the mean of l which can be calculated from:

$$\bar{l} = \frac{\sum_{i=1}^{n} l_i}{n}$$

The uncertainty of $\bar{l}$ ($\sigma_{\bar{l}}^2$) is calculated as:

$$\sigma_{\bar{l}}{}^2 = \frac{1}{n} \sum_{i=1}^{n} \sigma_{l_i}{}^2$$

where the σ_{l_i} denotes the uncertainty of LUE estimated for each biome type. The error propagation law allows us to calculate the uncertainties in CV of l as:

$$\sigma_{CV}{}^2 = \sum_{i=1}^{n} \left(\frac{\partial CV}{\partial l_i} \sigma_{l_i} \right)^2 + \left(\frac{\partial CV}{\partial \bar{l}} \sigma_{\bar{l}} \right)^2$$

$$= \sum_{j=1}^{n} \left(\frac{l_j - \bar{l}}{\bar{l}\sqrt{n-1}} \frac{1}{\sqrt{\sum_{i=1}^{n}(l_i - \bar{l})^2}} \sigma_{l_j} \right)^2$$

$$+ \left(\frac{1}{\sqrt{n-1}} \frac{\dfrac{\sum_{j=1}^{n}(\bar{l} - l_j)}{\sqrt{\sum_{i=1}^{n}(l_i - \bar{l})^2}} \bar{l} - \sqrt{\sum_{k=1}^{n}(l_k - \bar{l})^2}}{\bar{l}^2} \sigma_{\bar{l}} \right)^2$$

$$= \sum_{j=1}^{n} \left(\frac{1}{n-1} \left(\frac{l_j - \bar{l}}{\bar{l}} \right)^2 \frac{1}{\sum_{i=1}^{n}(l_i - \bar{l})^2} \sigma_{l_j}{}^2 \right) + \frac{1}{n-1} \frac{\sum_{k=1}^{n}(l_k - \bar{l})^2}{\bar{l}^4} \sigma_{\bar{l}}{}^2$$

6

Text S4. Land cover dataset for major biome types

The land cover classification is based on the IGBP classification scheme from the MCD12C1 C5 dataset for 2007 to 2013 (*Friedl et al.*, 2010). The MCD12C1 data have a spatial resolution of $0.05° \times 0.05°$, and for each gridcell, 16 numbers correspond to the areal percentages of 16 IGBP land cover types. We further aggregated this dataset to $0.5° \times 0.5°$ to match the spatial resolution of SIF and recalculated the areal percentages of 16 biome types for each $0.5° \times 0.5°$ gridcell. If one land cover type occupies more than 80% of the area of a $0.5° \times 0.5°$ gridcell, this gridcell is considered a "pure" pixel and further used for the biome-based statistical analysis (Fig. S11). 13 vegetated land cover types for both MCD12C1 and flux tower sites were aggregated into four major biome types. Forests include DBF, EBF, ENF, DNF, and MF. Shrublands include OSH, CSH, and WSA. Grasslands include GRA, SAV, and WET. Croplands include CRO and NVM. A full list of these acronyms can be found in Table S2.
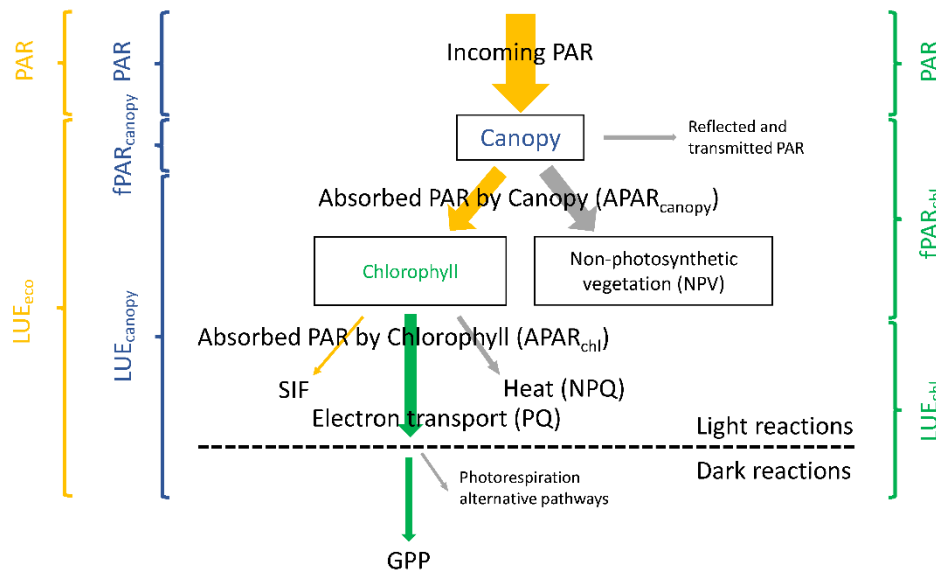
Figure S1. Idealized representation of the radiation partitioning in plant canopies for light use efficiency models. Left side is the LUE models based on the total PAR or PAR absorbed by canopy (APAR$_{canopy}$), right side is the LUE models based on PAR absorbed by chlorophyll of the entire canopy (fPAR$_{chl}$). This figure is modified from Fig. 1 in *Porcar-Castell et al.* (2014).
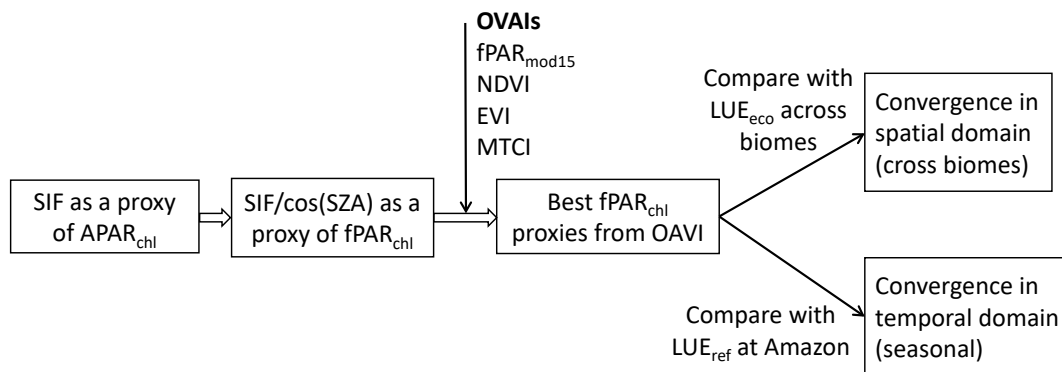

Figure S2. A flowchart showing the evaluation of spatio-temporal convergence of ε_{max} based on radiation absorption by chlorophylls of the canopy.
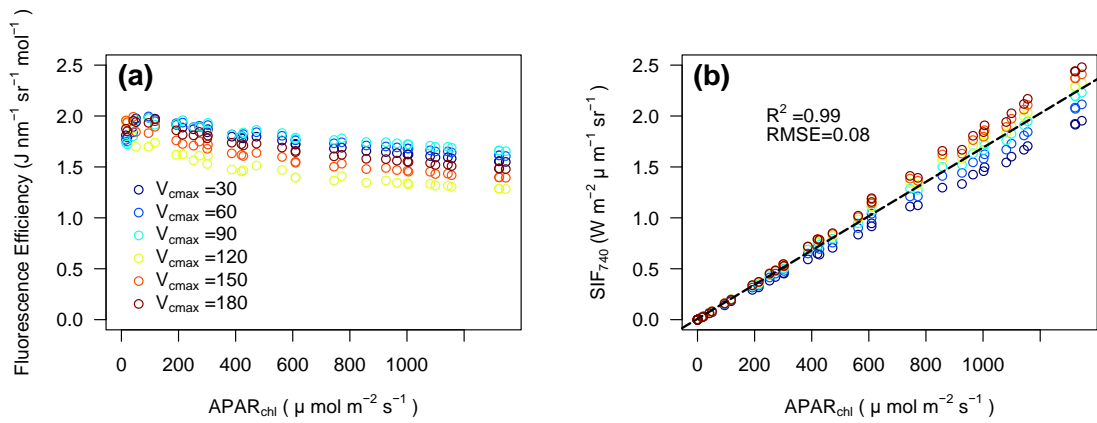
Figure S3. The relationship between (a) fluorescence efficiency and $APAR_{chl}$, and (b) SIF_{740} and $APAR_{chl}$ using the simulation from the SCOPE model.
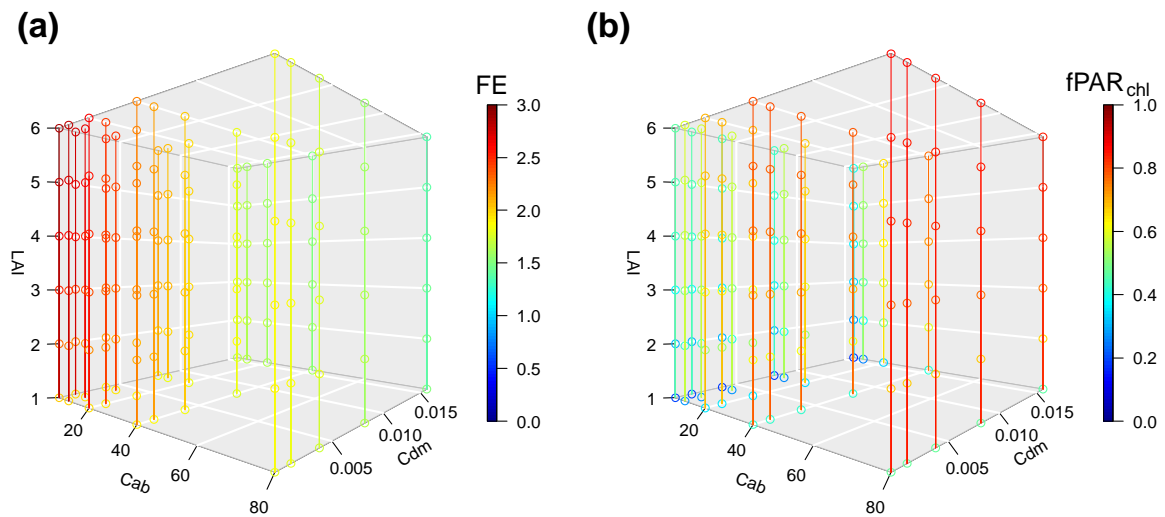
Figure S4. The variation of (a) fluorescence efficiency (in J nm^{-1} sr^{-1} mol^{-1}) and (b) $fPAR_{chl}$ under all possible combination of LAI, Cab and Cdm values in Table S6.
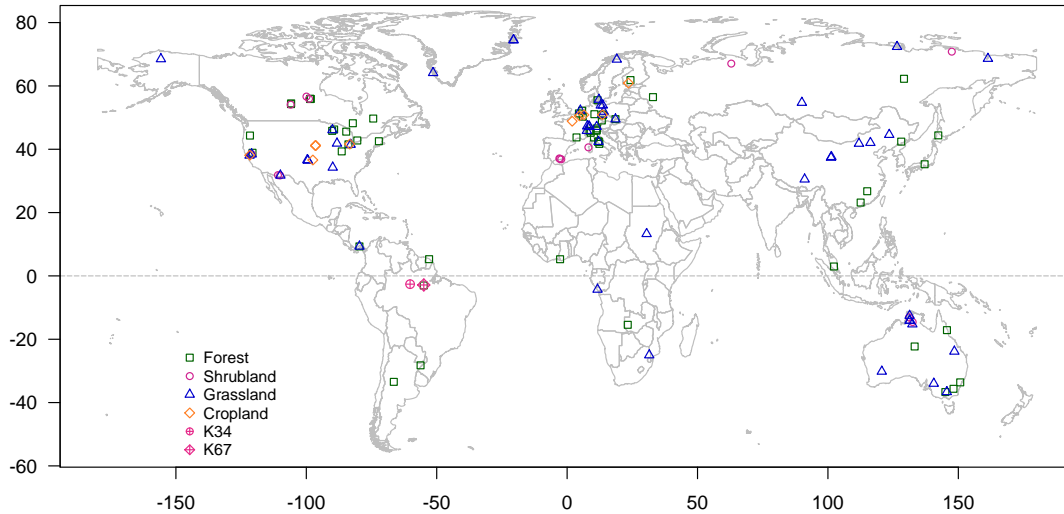
Figure S5. The spatial distribution of the flux tower sites used in this study. The biome types are regrouped into four types to correspond to the biome type in the SIF analysis. Forest includes ENF, EBF, DNF, DBF, and MF; shrubland includes CSH, OSH, and WSA; grassland includes SAV, GRA, WET; cropland includes CRO and CNV. For the full name of the vegetation types and the IGBP classification of land cover types, please refer to Table S2. K34 and K67 are two amazon sites used for seasonality analysis.
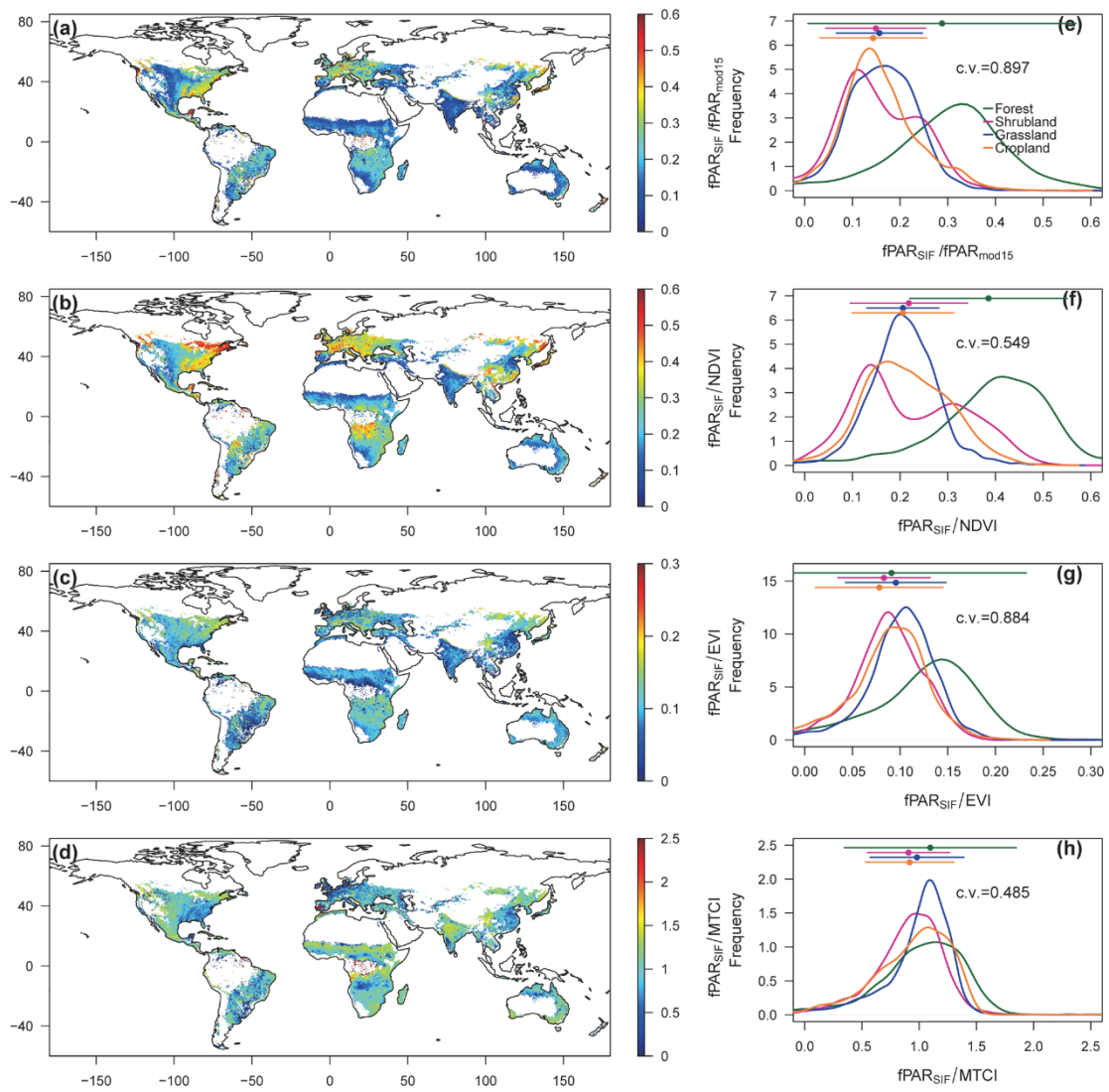
Figure S6. Spatial pattern (left column) and frequency distribution (right column) of the regression intercept (c in Eq. 6). (a, e) fPAR, (b, f) NDVI, (c, g) EVI, (d, h) MTCI. The dots with horizontal bars at the top of frequency distribution figures (e-h) represent the means and standard deviations within each biome type. The SIF and OVAIs data from 2007 to 2015 (2007–2012 for MTCI) were used to build the relationship.

11
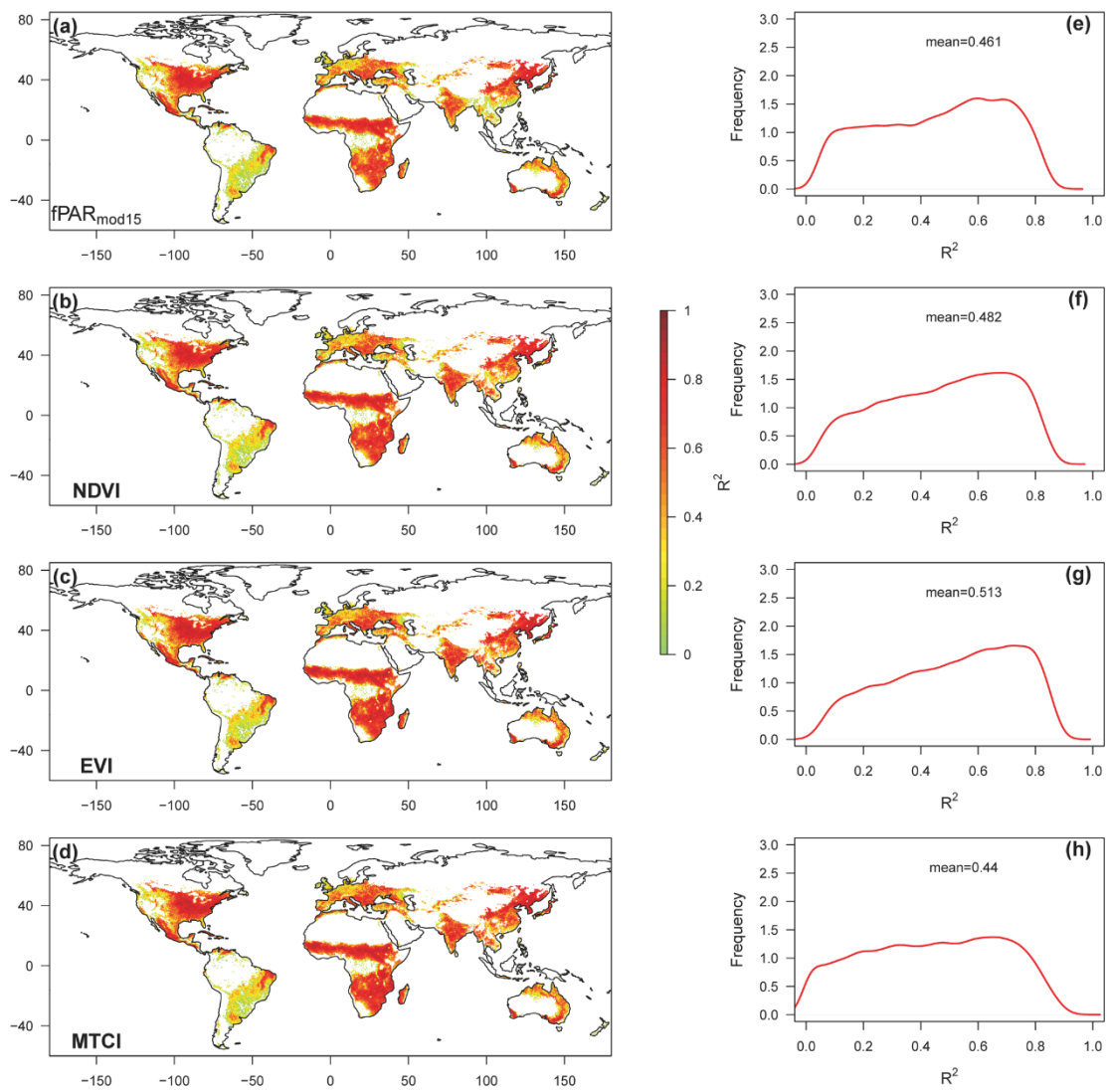
Figure S7. Spatial pattern (left column) and frequency distribution (right column) of the coefficient of determination (R^2) between $fPAR_{SIF}$ and four optical vegetation activity indicators (OVAIs). (a, e) fPAR, (b, f) NDVI, (c, g) EVI and (d, h) MTCI. The SIF and OVAIs data from 2007 to 2015 (2007−2012 for MTCI) were used to build the relationship. The low correlation coefficients in tropical regions are caused by high cloud cover and weak seasonality of vegetation.

12
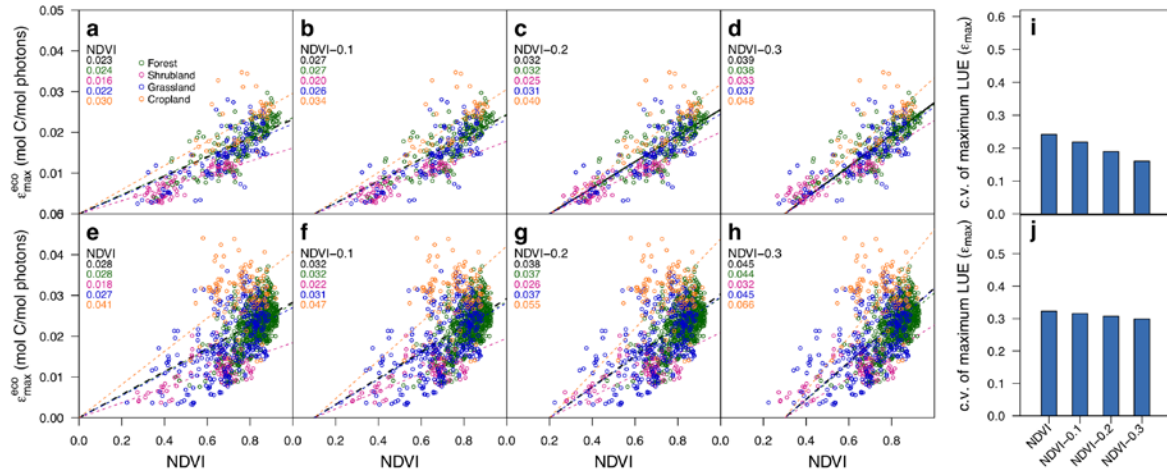
Figure S8. Estimation of maximum daily light use efficiency (regression slopes) based on different fPAR-NDVI relationship (with different intercept) for clear-day (a-d) and cloudy-day (e-h). The coefficient of variation of maximum light use efficiency across biome types for clear-day (i) and cloudy-day (j).
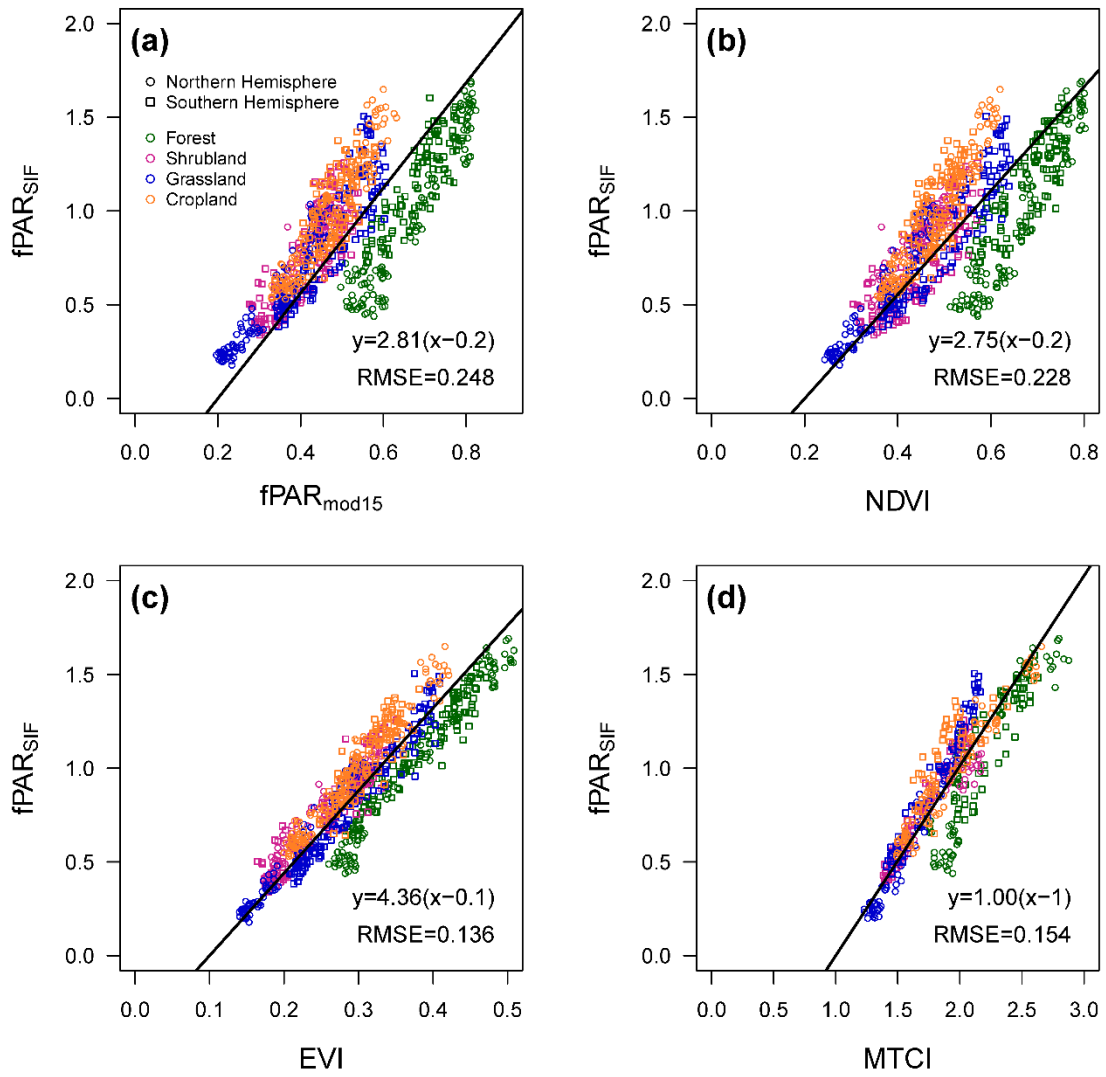
Figure S9. The linear regression with fixed OVAI intercept, same dataset from Fig. 1 is used. The RMSE value were used as the uncertainty of regression for error propagation analysis.
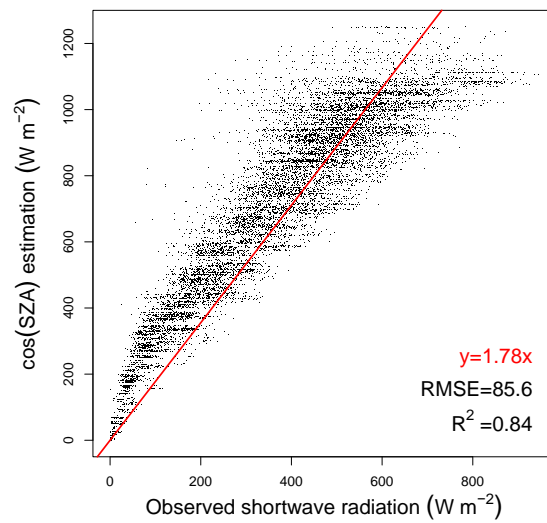
Figure S10. Comparison between the estimated iPAR at 9:30 am using cos(SZA) and observed iPAR from flux tower sites. This comparison used monthly averaged iPAR values to match the temporal resolution of GOME2 SIF product. Altogether 127 sites were used.
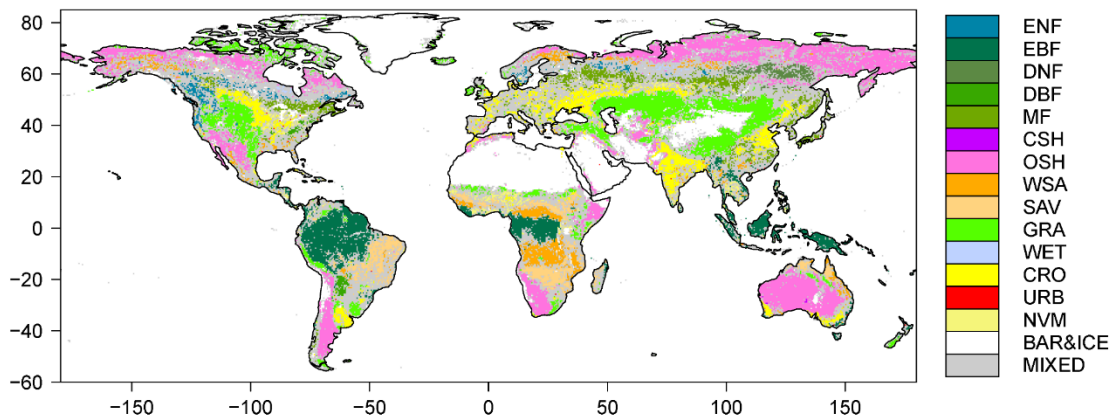
Figure S11. The land cover type at the resolution of $0.5° \times 0.5°$ for year 2007. Only the "pure" pixels which are used for further analysis are shown. White areas are barren and ice covered; grey are mixed pixels. For a complete list of the legend acronyms, please refer to Table S2.

OVAIs	Product	Calculation	Original spatial resolution	Temporal resolution	Data quality check	Uncertainty (absolute value)	Spatial extent
$fPAR_{mod15}$	MOD15A2H C6	spectral information from MODIS surface reflectance at 648 nm and 858 nm and radiative transfer equation based Look-up-Table	500 m	8-day	both MOD09A1 QA and MOD15A2H QA	0.15^{1}	global
NDVI	MOD09A1 C6 for site, MOD13C2 C6 for regional	$\dfrac{\rho_{858.5} - \rho_{645}}{\rho_{858.5} + \rho_{645}}$	500 m	8-day for site, monthly for regional	MOD09A1 QA for site, MOD13C2 Pixel Reliability for regional	0.025^{2}	global
EVI	MOD09A1 C6 for site, MOD13C2 C6 for regional	$2.5\dfrac{\rho_{858.5} - \rho_{645}}{1 + \rho_{858.5} + 6\rho_{645} - 7.5\rho_{469}}$	500 m	8-day for site, monthly for regional	MOD09A1 QA for site, MOD13C2 Pixel Reliability for regional	0.015^{2}	global
MTCI	NEODC MTCI Level 3	$\dfrac{\rho_{753.75} + \rho_{708.75}}{\rho_{708.75} - \rho_{681.25}}$	~5000 m	8-day for 2002-2007, 10-day for 2008-2012	N/A	0.1^{3}	180°W-180°E, 80°S-80°N

[1]*Yan et al.* (2016); [2]https://landval.gsfc.nasa.gov/ProductStatus.php?ProductID=MOD13; [3]*Elsobky* (2015), this number is a rough estimate across different biomes.

Table S1. Optical vegetation activity indices (OVAIs) used in this study. ρ with a subscription number indicate the satellite retrieved band reflectance centered at this wavelength.

Site ID	Site name	Latitude	Longitude	Country	IGBP type	Years used
AR-SLu	San Luis	-33.4648	-66.4598	Argentina	MF	2010
AR-Vir	Virasoro	-28.2395	-56.1886	Argentina	ENF	2012
AT-Neu	Neustift/Stubai Valley	47.1167	11.3175	Austria	GRA	2002-2005, 2007-2009, 2011
AU-Ade	Adelaide River	-13.0769	131.1178	Australia	WSA	2007-2009
AU-ASM	Alice Springs	-22.283	133.249	Australia	ENF	2010-2012
AU-Cpr	Calperum	-34.0021	140.5891	Australia	SAV	2011-2013
AU-Cum	Cumberland Plains	-33.6133	150.7225	Australia	EBF	2013
AU-DaP	Daly River Savanna	-14.0633	131.3181	Australia	GRA	2008-2011, 2013
AU-DaS	Daly River Cleared	-14.1593	131.3881	Australia	SAV	2008, 2009, 2011-2013
AU-Dry	Dry River	-15.2588	132.3706	Australia	SAV	2010-2013
AU-Emr	Emerald, Queensland, Australia	-23.8587	148.4746	Australia	GRA	2011-2013
AU-Fog	Fogg Dam	-12.5452	131.3072	Australia	WET	2007, 2008
AU-GWW	Great Western Woodlands, Western Australia, Australia	-30.1913	120.6541	Australia	SAV	2013
AU-RDF	Red Dirt Melon Farm, Northern Territory	-14.5636	132.4776	Australia	WSA	2011, 2012
AU-Rig	Riggs Creek	-36.6499	145.5759	Australia	GRA	2012, 2013
AU-Rob	Robson Creek, Queensland, Australia	-17.1175	145.6301	Australia	EBF	2014
AU-Tum	Tumbarumba	-35.6566	148.1517	Australia	EBF	2004, 2006-2013
AU-Whr	Whroo	-36.6732	145.0294	Australia	EBF	2012, 2013
BE-Bra	Brasschaat (De Inslag Forest)	51.3092	4.5206	Belgium	MF	2000, 2005-2009, 2011-2013
BE-Lon	Lonzee	50.5516	4.7461	Belgium	CRO	2004, 2005, 2007-2009, 2011-2013
BE-Vie	Vielsalm	50.3051	5.9981	Belgium	MF	2002, 2003, 2005-2010, 2012-2014
BR-Sa3	Santarem-Km83-Logged Forest	-3.018	-54.9714	Brazil	EBF	2001-2003

CA-Gro	Ontario - Groundhog River, Boreal Mixedwood Forest.	48.2167	-82.1556	Canada	MF	2004-2009, 2013
CA-NS1	UCI-1850 burn site	55.8792	-98.4839	Canada	ENF	2002-2005
CA-NS3	UCI-1964 burn site	55.9117	-98.3822	Canada	ENF	2004, 2005
CA-NS4	UCI-1964 burn site wet	55.9117	-98.3822	Canada	ENF	2003-2005
CA-NS5	UCI-1981 burn site	55.8631	-98.485	Canada	ENF	2002-2005
CA-NS6	UCI-1989 burn site	55.9167	-98.9644	Canada	OSH	2002, 2004, 2005
CA-NS7	UCI-1998 burn site	56.6358	-99.9483	Canada	OSH	2002, 2004, 2005
CA-Qfo	Quebec - Eastern Boreal, Mature Black Spruce.	49.6925	-74.3421	Canada	ENF	2004-2006, 2008-2010
CA-SF1	Saskatchewan - Western Boreal, forest burned in 1977.	54.485	-105.818	Canada	ENF	2003, 2005, 2006
CA-SF2	Saskatchewan - Western Boreal, forest burned in 1989.	54.2539	-105.878	Canada	ENF	2002-2005
CA-SF3	Saskatchewan - Western Boreal, forest burned in 1998.	54.0916	-106.005	Canada	OSH	2001, 2003-2006
CA-TP2	Ontario - Turkey Point 1989 Plantation White Pine	42.7744	-80.4588	Canada	ENF	2003-2005
CG-Tch	Tchizalamou	-4.2892	11.6564	Republic of Congo	SAV	2006, 2007, 2009
CH-Cha	Chamau grassland	47.2102	8.4104	Switzerland	GRA	2007, 2008, 2010-2012
CH-Fru	Fruebuel grassland	47.1158	8.5378	Switzerland	GRA	2007, 2008, 2010-2012
CH-Oe1	Oensingen1 grass	47.2858	7.7319	Switzerland	GRA	2002-2008
CN-Cha	Changbaishan	42.4025	128.0958	China	MF	2003-2005
CN-Cng	Changling	44.5934	123.5092	China	GRA	2008, 2010
CN-Dan	Dangxiong	30.4978	91.0664	China	GRA	2004, 2005
CN-Din	Dinghushan	23.1733	112.5361	China	EBF	2003, 2005
CN-Du2	Duolun_grassland (D01)	42.0467	116.2836	China	GRA	2008
CN-Ha2	Haibei Shrubland	37.6086	101.3269	China	WET	2003-2005
CN-HaM	Haibei Alpine Tibet site	37.6167	101.3	China	GRA	2002, 2003

CN-Qia	Qianyanzhou	26.7414	115.0581	China	ENF	2003-2005
CN-Sw2	Siziwang Grazed (SZWG)	41.7902	111.8971	China	GRA	2011
CZ-BK1	Bily Kriz- Beskidy Mountains	49.5047	18.5411	Czech Republic	ENF	2003-2005, 2007-2012
CZ-BK2	Bily Kriz- grassland	49.4944	18.5429	Czech Republic	GRA	2006-2011
DE-Akm	Anklam	53.8662	13.6834	Germany	WET	2011-2013
DE-Gri	Grillenburg- grass station	50.9495	13.5125	Germany	GRA	2004-2006, 2008-2014
DE-Hai	Hainich	51.0792	10.453	Germany	DBF	2000-2005, 2007-2009, 2012
DE-Kli	Klingenberg - cropland	50.8929	13.5225	Germany	CRO	2004-2006, 2009, 2010, 2014
DE-Lkb	Lackenberg	49.0996	13.3047	Germany	ENF	2009, 2012, 2013
DE-Obe	Oberbarenburg	50.7836	13.7196	Germany	ENF	2008-2014
DE-RuS	Selhausen Juelich	50.8657	6.4472	Germany	CRO	2011-2014
DE-Spw	Spreewald	51.8923	14.0337	Germany	WET	2010-2012, 2014
DE-Tha	Anchor Station Tharandt - old spruce	50.9636	13.5669	Germany	ENF	2000, 2001, 2003-2005, 2007-2014
DE-Zrk	Zarnekow	53.8759	12.889	Germany	WET	2013, 2014
DK-Eng	Enghave	55.6905	12.1918	Denmark	GRA	2005
DK-NuF	Nuuk Fen	64.1308	-51.3861	Denmark	WET	2008, 2010, 2012-2014
DK-Sor	Soroe-LilleBogeskov	55.4859	11.6446	Denmark	DBF	2000, 2002-2012
DK-ZaF	Zackenberg Fen	74.4791	-20.5557	Denmark	WET	2008, 2010, 2013, 2014
DK-ZaH	Zackenberg Heath	74.4732	-20.5503	Denmark	GRA	2002, 2003, 2005, 2006, 2008
ES-Amo	Amoladeras	36.8336	-2.2523	Spain	OSH	2010, 2011
ES-LgS	Laguna Seca	37.0979	-2.9658	Spain	OSH	2007-2009
ES-LJu	Llano de los Juanes	36.9266	-2.7521	Spain	OSH	2004, 2006, 2008, 2010, 2011, 2013
FI-Hyy	Hyytiala	61.8475	24.295	Finland	ENF	2000, 2001, 2003-2005, 2008-2014
FI-Jok	Jokionen agricultural field	60.8986	23.5135	Finland	CRO	2001, 2003
FR-Gri	Grignon (after 6/5/2005)	48.8442	1.9519	France	CRO	2005-2011, 2014

FR-Pue	Puechabon	43.7414	3.5958	France	EBF	2001-2012
GF-Guy	Guyaflux	5.2788	-52.9249	French Guyana	EBF	2004-2006, 2008-2012
GH-Ank	Ankasa	5.2685	-2.6942	Ghana	EBF	2011, 2012, 2014
IT-CA1	Castel d'Asso1	42.3804	12.0266	Italy	DBF	2011, 2012
IT-CA2	Castel d'Asso2	42.3772	12.026	Italy	GRA	2011, 2013
IT-CA3	Castel d'Asso 3	42.38	12.0222	Italy	DBF	2013
IT-Cp2	Castelporziano2	41.7043	12.3573	Italy	EBF	2013
IT-Isp	Ispra ABC-IS	45.8126	8.6336	Italy	DBF	2014
IT-La2	Lavarone2	45.9542	11.2853	Italy	ENF	2001
IT-Lav	Lavarone (after 3/2002)	45.9562	11.2813	Italy	ENF	2003-2011
IT-Noe	Sardinia/Arca di Noè	40.6061	8.1515	Italy	CSH	2004-2008, 2010
IT-PT1	Zerbolo-Parco Ticino- Canarazzo	45.2009	9.061	Italy	DBF	2002, 2004
IT-Ren	Renon/Ritten (Bolzano)	46.5869	11.4337	Italy	ENF	2001, 2002, 2004-2010, 2012, 2013
IT-Ro1	Roccarespampani 1	42.4081	11.93	Italy	DBF	2001-2004, 2006-2008
IT-Ro2	Roccarespampani 2	42.3903	11.9209	Italy	DBF	2002-2008, 2010, 2012
IT-SRo	San Rossore	43.7279	10.2844	Italy	ENF	2002, 2003, 2006-2012
IT-Tor	Torgnon	45.8444	7.5781	Italy	GRA	2008-2010, 2012, 2013
JP-MBF	Moshiri Birch Forest Site	44.3869	142.3186	Japan	DBF	2004
JP-SMF	Seto Mixed Forest Site	35.2617	137.0788	Japan	MF	2003, 2005, 2006
MY-PSO	Pasoh Forest Reserve (PSO)	2.973	102.3062	Malaysia	EBF	2003-2009
NL-Hor	Horstermeer	52.2404	5.0713	Netherlands	GRA	2005, 2007, 2008, 2010
NL-Loo	Loobos	52.1666	5.7436	Netherlands	ENF	2000-2002, 2004-2014
PA-SPn	Sardinilla Plantation	9.3181	-79.6346	Panama	DBF	2007, 2008
RU-Che	Cherskii	68.613	161.3414	Russia	WET	2002-2004
RU-Cok	Chokurdakh	70.8291	147.4943	Russia	OSH	2003, 2006, 2007, 2009, 2011, 2012
RU-Fyo	Fyodorovskoye wet spruce stand	56.4615	32.9221	Russia	ENF	2000-2006, 2008, 2009, 2011-2013
RU-Ha1	Ubs Nur- Hakasija- grassland	54.7252	90.0022	Russia	GRA	2003, 2004

RU-Sam	Samoylov Island-Lena Delta	72.3738	126.4958	Russia	GRA	2005, 2006, 2008
RU-SkP	Spasskaya Pad larch	62.255	129.168	Russia	DNF	2012-2014
RU-Vrk	Seida/Vorkuta	67.0547	62.9405	Russia	CSH	2008
SD-Dem	Demokeya	13.2829	30.4783	Sudan	SAV	2007-2009
SE-St1	Stordalen Forest-Mountain Birch	68.3542	19.0503	Sweden	WET	2012, 2014
US-ARM	ARM Southern Great Plains site-Lamont	36.6058	-97.4888	USA	CRO	2003, 2004, 2006-2010, 2012
US-Blo	Blodgett Forest	38.8953	-120.633	USA	ENF	2003, 2004, 2006, 2007
US-CRT	Curtice Walter-Berger cropland	41.6285	-83.3471	USA	CRO	2011-2013
US-Goo	Goodwin Creek	34.2547	-89.8735	USA	GRA	2002-2004, 2006
US-Ha1	Harvard Forest EMS Tower (HFR1)	42.5378	-72.1715	USA	DBF	2000, 2001, 2003-2012
US-Ivo	Ivotuk	68.4865	-155.75	USA	WET	2004, 2006, 2007
US-Los	Lost Creek	46.0827	-89.9792	USA	WET	2001-2008, 2010, 2014
US-Me6	Metolius Young Pine Burn	44.3233	-121.608	USA	ENF	2010-2012
US-MMS	Morgan Monroe State Forest	39.3232	-86.4131	USA	DBF	2000-2006, 2009, 2010, 2013, 2014
US-Myb	Mayberry Wetland	38.0498	-121.765	USA	WET	2011-2014
US-Ne2	Mead - irrigated maize-soybean rotation site	41.1649	-96.4701	USA	CRO	2002, 2004, 2006, 2008
US-Ne3	Mead - rainfed maize-soybean rotation site	41.1797	-96.4397	USA	CRO	2002, 2004, 2006, 2008, 2010, 2012
US-Oho	Oak Openings	41.5545	-83.8438	USA	DBF	2004-2011, 2013
US-SRM	Santa Rita Mesquite	31.8214	-110.866	USA	WSA	2004-2008, 2010-2014
US-Syv	Sylvania Wilderness Area	46.242	-89.3477	USA	MF	2002, 2012-2014
US-Ton	Tonzi Ranch	38.4316	-120.966	USA	WSA	2002-2007, 2009, 2012-2014
US-Tw3	Twitchell Alfalfa	38.1159	-121.647	USA	CRO	2013, 2014
US-UMd	UMBS Disturbance	45.5625	-84.6975	USA	DBF	2008-2014
US-Var	Vaira Ranch- Ione	38.4133	-120.951	USA	GRA	2000-2007, 2009, 2011-2014

US-WCr	Willow Creek	45.8059	-90.0799	USA	DBF	2000, 2001, 2003-2006, 2011, 2013, 2014
US-Whs	Walnut Gulch Lucky Hills Shrub	31.7438	-110.052	USA	OSH	2007, 2008, 2010, 2011, 2013, 2014
US-Wkg	Walnut Gulch Kendall Grasslands	31.7365	-109.942	USA	GRA	2006-2008, 2010-2014
US-WPT	Winous Point North Marsh	41.4646	-82.9962	USA	WET	2011-2013
ZA-Kru	Skukuza- Kruger National Park	-25.0197	31.4969	South Africa	SAV	2000, 2009-2012
ZM-Mon	Mongu	-15.4378	23.2528	Zambia	DBF	2007-2009

Table S2. Flux tower sites used in this study. ENF: evergreen needleleaf forest; EBF: evergreen broadleaf forest; DNF: deciduous needleleaf forest; DBF: deciduous broadleaf forest; MF: mixed forest; CSH: closed shrubland; OSH: open shrubland; WSA: woody savannas; GRA: grassland; SAV: savannas; WET: permanent wetland; CRO: cropland; CNV: cropland/natural vegetation mosaic.

Variables	Estimated from	Uncertainty (represented as s.d. or RMSE)
iPAR	cos(SZA)	85.6 W m^{-2}
fPAR$_{SIF}$[1]	SIF	0.34
OVAI$_m$[2] (approximation of fPAR$_{chl}$ using OVAI)	fPAR$_{mod15}$	0.17 (0.11)
	NDVI	0.09 (0.08)
	EVI	0.03 (0.03)
	MTCI	0.18 (0.16)

[1]fPAR$_{SIF}$ considered the uncertainty of FE. [2]These uncertainties are estimated for the 8-day (10-day) temporal resolution, the values in the parentheses are adjusted for peak growing season period (five 8-day or four 10-day) to compare with LUE$_{eco}$.

Table S3. The uncertainties of approximations used in our study.

	fPAR	NDVI	EVI$_m$	MTCI$_m$
clear	0.00722	0.00661	0.00551	0.00541
cloudy	0.00692	0.00653	0.00671	0.00590

Table S4. Root mean square error (RMSE) for the regressions between LUE$_{PAR}$ and OVAI or OVAI$_m$, with all biome types combined together.

	fPAR	NDVI	EVI$_m$	MTCI$_m$
clear	0.40	0.49	0.64	0.69

cloudy	0.20	0.29	0.25	0.40

Table S5. Coefficient of determination (R^2) for the regressions between LUE_{PAR} and OVAI or $OVAI_m$, with all biome types combined together.

Parameter	Symbol	Value	Range
Chlorophyll a+b content [µg cm-2]	Cab	0.001, 0.002, 0.004, 0.008, 0.016	0.001 - 0.02
Dry matter content [g cm-2]	Cdm	0.001, 0.002, 0.004, 0.008, 0.016, 0.032, 0.064	0.001 - 0.05
Leaf area index [m2 m-2]	LAI	1, 2, 3, 4, 5, 6	1 - 6

Table S6. Parameters settings used in the second run of the SCOPE model with fixed irradiance but variable parameters which result in different f_{esc} values.